Nano Research

Open Access

Research Article

Adaptive hexagonal metal-oxynitride monolayers for oxygen reduction catalysis

Xin Lei[1,2,§], Ruihui Gan[1,§], Xiaodong Shao[3], Jinxiao Wu[1], Yongping Zheng[1,4] ✉, Chunlei Jiang[1,2], and Yongbing Tang[1,2] ✉

[1] *Advanced Energy Storage Technology Research Center, Shenzhen Institutes of Advanced Technology, Chinese Academy of Sciences, Shenzhen 518055, China*
[2] *University of Chinese Academy of Sciences, Beijing 100049, China*
[3] *Department of Chemistry, Sungkyunkwan University, Suwon 16419, Republic of Korea*
[4] *Guangdong Provincial Key Laboratory of New Energy Materials Service Safety, College of Materials Science and Engineering, Shenzhen University, Shenzhen 518060, China*
[§] *Xin Lei and Ruihui Gan contributed equally to this work.*

Cite this article: *Nano Research*, **2026**, *19*, 94908558. https://doi.org/10.26599/NR.2026.94908558

ABSTRACT: Transition metal nitrides (TMNs) have recently attracted increasing attention as a robust alternative to platinum electrocatalysts in alkaline oxygen reduction reaction (ORR). However, the fundamental understanding of the catalytic nature of the TMNs remains elusive, impeding the further catalyst design and optimization. Here, using ZrN as a model catalyst, we demonstrate that the unexpected catalytic activity of TMNs originates from the self-adaptive behavior of surface-reconstructed oxynitride monolayers under ORR conditions. Our first-principles calculations reveal that oxygen adsorption triggers a square-to-hexagonal symmetry transition on the ZrN surface, stabilizing a hexagonal ZrNO monolayer. At quarter-hydroxyl coverage, this reconstruction generates semi-elliptical cavities that confine the highly active Zr sites. Crucially, the flexible Zr–N–Zr linkages connecting these Zr sites and the underlying ZrN substrate undergo dynamic bond-length variations during ORR, which precisely regulate oxygen intermediate adsorption and significantly enhance catalytic activity. Experimental characterization aligns well with these theoretical predictions. The as-designed ZrNO monolayer catalyst delivers a 0.882 V half-wave potential for ORR and enables zinc–air batteries with 240 mW·cm^{-2} peak power density—metrics that exceed state-of-the-art Pt/C. This study provides atomic-level insights into the nature of TMNs' catalytic monolayers, paving the way for stable and active catalyst engineering in next-generation energy technologies.

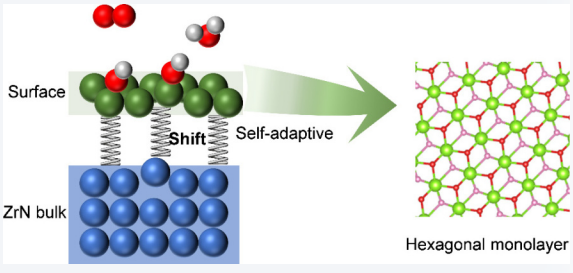

KEYWORDS: self-adaptive, hexagonal monolayer, transition metal oxynitride, oxygen reduction reaction

1 Introduction

The development of advanced and inexpensive electrocatalysts for sluggish oxygen reduction reaction (ORR) is critical to anion exchange membrane fuel cells and metal–air batteries [1–6]. These two clean energy technologies are currently hindered by the scarce and expensive noble Pt electrocatalysts (37 ppb in Earth's crust and 32.3 USD·g^{-1} as the 2023 average price), which represent the state-of-the-art ORR electrocatalysts [7, 8]. Extensive efforts have been devoted to Pt alternatives in the hope that they will reduce the use of platinum or even replace it, and some important advances have been made both experimentally and theoretically [9–15]. Among them, transition metal nitrides (TMNs) have aroused considerable attention in electrocatalytic ORR owing to their low costs, high conductivity, and stability [16–23]. However, the origins of the TMNs' activity in the ORR remain in debate, that is, whether its ORR activity is determined by the intrinsic electronic structure or the surface structural evolution during the electrocatalytic process, which severely limits their further optimization for practical applications [24–27]. Therefore, revealing the catalytic nature of TMNs in ORR is vital to promote the development of stable and active electrocatalysts with transition metal compounds [28–30].

Recently, Zeng et al. reported that constructing oxide catalytic

Received: November 5, 2025; **Revised:** January 15, 2026
Accepted: February 11, 2026

✉Address correspondence to Yongping Zheng, ypzheng@szu.edu.cn; Yongbing Tang, tangyb@siat.ac.cn

layers on TMNs, such as MnN@Mn_3O_4 core–shell structure [31], can significantly enhance ORR activity compared to their individual components, even rivaling the performance of state-of-the-art Pt/C catalysts. Notably, the outermost catalytic thin layers, strained by the underlying TMN supports, have been identified as the key factor responsible for their superior intrinsic ORR activity over their pure-phase counterparts [32–37]. This important finding suggests that atomic-level reconstruction of TMN surface layers could enable the design of highly active ORR catalysts, combining exceptional stability with the inherent advantages of TMNs. While oxidation-prone TMNs like MnN readily undergo surface reconstruction into active oxide overlayers under reaction conditions, their corrosion resistance remains intrinsically limited by the instability of the parent TMN matrix [38, 39]. In contrast, zirconium nitride (ZrN) demonstrates exceptional corrosion resistance, high-temperature stability, and excellent electrical conductivity—properties that overcome the durability limitations of conventional TMN catalysts [40–43]. However, this remarkable stability presents a unique challenge: The ultra-robust atomic structure of ZrN resists conventional surface reconstruction pathways that typically create active sites in less stable TMNs (e.g., MnN) [44, 45]. This suggests the potential existence of novel reconstruction mechanisms, possibly involving monolayer (ML) surface restructuring, which could activate the catalytic potential of ZrN while maintaining its corrosion-resistant bulk properties. Combined with the key ORR mechanistic insights on Zr-based materials by implementing the strategy of modifying nitride surfaces with oxy/hydroxy species, the ZrN surface construction could overcome the inefficient O–O bond cleavage typical of conventional ZrO_x surfaces [46, 47].

In this work, we systematically investigate the dynamic surface reconstruction of ZrN through combined first-principles calculations and experimental validation, resolving the long-standing controversy regarding the origin of ORR activity in ZrN-based catalysts. Our computational results demonstrate that oxygen adsorption triggers spontaneous reconstruction of ZrN surface square cells into hexagonal ZrNO units, with subsequent quart-monolayer hydroxyl incorporation driving further evolution into ZrNO–OH structures featuring semi-elliptical cavities. These unique cavities confine highly active Zr sites facilitate rapid oxygen intermediate transformation via self-adaptive Zr–N–Zr bond linkages connecting these Zr sites and the ZrN sublayer. To verify these predictions, we developed an innovative organobase-induced surface reconstruction strategy. The resulting ZrN@ZrNO–OH electrocatalyst exhibits excellent structural agreement with our theoretical models, demonstrating superior ORR activity with a half-wave potential of 0.882 V and enhanced zinc–air battery performance (peak power density: 240 mW·cm^{-2}) compared to pristine ZrN. This work elucidates the fundamental catalytic mechanism of TMNs through controlled surface monolayer reconstruction, establishing a general design principle for developing exceptionally stable yet highly active earth-abundant TMN electrocatalysts.

2 Results and discussion

2.1 Theoretical investigation

To investigate the ORR activity of unreconstructed ZrN surface, we performed density functional theory (DFT) calculations based on the adsorbate evolution mechanism (Fig. 1(a) and Fig. S1 in the Electronic Supplementary Material (ESM)). It is found that the ORR performance of pristine ZrN is kinetically limited by the *O hydrogenation step (*O → *OH), where the strong binding of *O species to Zr surface sites results in a suboptimal hydrogenation exothermicity (Gibbs free energy change (ΔG) = −0.41 eV), thereby restricting overall catalytic activity. Given this energetic bottleneck, *O intermediates are likely to accumulate on the pristine ZrN surface. Furthermore, oxygen adsorption studies (Figs. 1(b) and 1(c)) demonstrate that the ZrN surface can readily achieve oxygen coverages of 1/8, 1/4, 1/2, and even full monolayer coverage, with highly exothermic adsorption energies exceeding −2.5 eV in all cases.

Impressively, in the full oxygen coverage, the surface regular ZrN monolayer with octahedron ZrN_6 unit (Fig. 1(d)) self-reconstructs into a hexagonal ZrNO monolayer with trigonal antiprism ZrN_3O_3 unit (C_{3v} point group). This is because the ZrN_6 unit of the cubic ZrN crystal possesses a highly structural symmetry (O_h point group), whereas the oxygen adsorbed on the Zr site leads to the stronger chemisorption interaction between oxygen and Zr atoms within the ZrN_6 unit, and therefore formation of a distorted octahedron ZrN_5O unit with decreased symmetry (C_{4v} point group). This instability, unsymmetric structural characteristic of the ZrN_5O unit, results in much higher formation energy than the pristine ZrN_6 unit, increased from the −3.17 eV of the ZrN_6 unit to the −2.48 eV of the ZrN_5O unit (Fig. S2 in the ESM). To release the excess energy, the distortion octahedron ZrN_5O unit is necessary to occur structural rearrangement, and therefore, a trigonal antiprism ZrN_3O_3 unit with a much lower formation energy of −4.50 eV is obtained, and then close-packed into a stable hexagonal ZrNO monolayer. In crystallography, the trigonal antiprism ZrN_3O_3 unit of the hexagonal ZrNO monolayer evolved from the distorted octahedron ZrN_5O unit, with the Zr coordination center remaining six-coordinate. Therefore, the Zr atom situated in the nitrogen atom plane center of the ZrN_5O unit is lifted approximately by 0.54 Å to reconfigure into ZrN_3O_3 unit. Consequently, the distance between the surface reconstruction hexagonal ZrNO monolayer and the ZrN sub-layer expands to 2.85 Å, which is higher than that of the 2.31 Å of the pristine ZrN. *Ab initio* molecular dynamic (AIMD) calculation was performed to illustrate the structural stability of the surface reconstruction hexagonal ZrNO monolayer connected with the bulk ZrN. The energy and the temperature of the system comprised of the bulk ZrN and surface hexagonal ZrNO monolayer show a well robust within a 3 ps trajectory (Figs. S3 and S4 in the ESM), and the Zr–N and Zr–O bond lengths of the ZrNO monolayer show a dynamic equilibrium (Fig. S5 in the ESM), both of which suggest that the hexagonal configuration of the ZrNO monolayer can be well-preserved in the ambient condition.

To clarify how the surface reconstruction hexagonal ZrNO monolayer affects the ORR under alkaline conditions, we investigated the pre-adsorption behavior of hydroxide on the ZrNO monolayer, subject to different hydroxide coverage (0, 1/8, 1/4, 3/8, 1/2, and 1 ML-OH) (Fig. S6 in the ESM). Unexpectedly, in the alkaline ORR conditions, the strong coordinate ability of hydroxides causes the surface ZrNO monolayer to further reconstruct into the ZrNO–OH monolayer (Fig. 2(a)), which retains the hexagonal configuration and consists of reconfigured tetrahedron ZrO_3-OH units and the intrinsic trigonal antiprism ZrN_3O_3 units. In addition, the adsorbed hydroxyl group applies an upward force to the adsorbed Zr site, resulting in the Zr center of

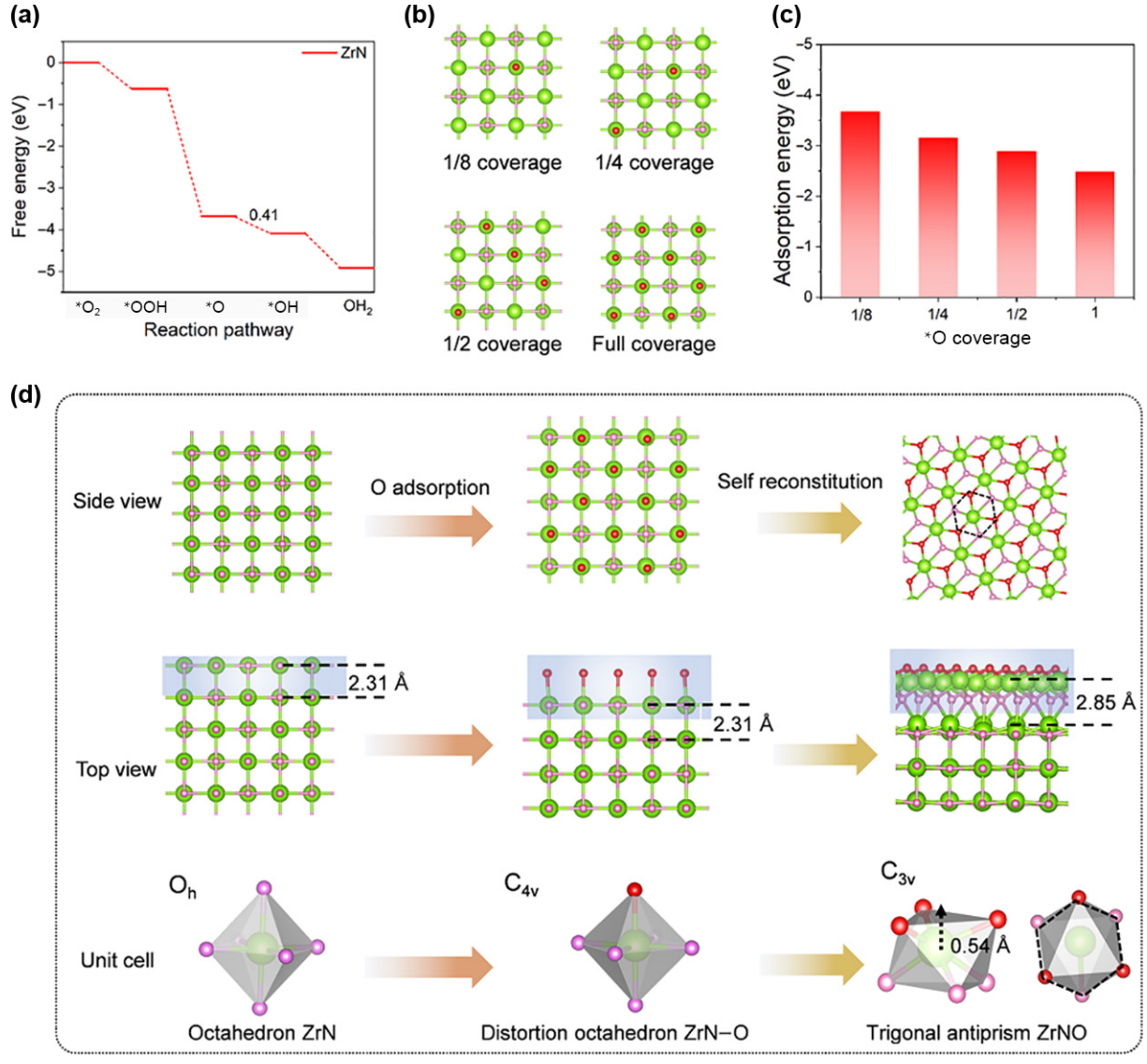

Figure 1 (a) The ORR Gibbs free energy diagram of ZrN. ((b) and (c)) Structural schematics of (b) ZrN with 1/8, 1/4, 1/2, and full oxygen coverage and (c) the corresponding adsorption energy. (d) The top view, side view, and unit cell diagrams of the octahedron ZrN, distortion octahedron ZrN–O, and trigonal antiprism ZrNO (green: Zr atom; red: O atom; pink: N atom; and grey: H atom).

the ZrO_3-OH unit being lifted by 1.45 Å from the Zr atom plane of the ZrN_3O_3 unit. The maximum hydroxide coverage on ZrNO was determined to be 3/8 ML-OH, further increased to 1/2 ML-OH and 1 ML-OH causing the collapse of the skeleton of the tetrahedron ZrO_3-OH unit due to the formation of hydrogen framework (circled in black in Fig. S6 in the ESM). Therefore, in the following calculations, we only considered the ORR process of ZrNO in the conditions of 0, 1/8, 1/4, and 3/8 ML-OH, implying only a partial of the intrinsic trigonal antiprism ZrN_3O_3 unit of the reconstruction ZrNO monolayer could further reconstruct into tetrahedron ZrO_3-OH unit.

The hydration of the adsorbed *OH intermediate into the H_2O product is revealed to be the rate-determining step (RDS) of the pristine ZrNO monolayer (Fig. S7 in the ESM), which imposes a significant restriction on the ORR activity of the ZrNO monolayer due to its low exothermicity (ΔG = −0.17 eV). This awkward situation is mitigated by the hydroxide, which brings the ZrO_3-OH units into the reconstruction hexagonal ZrNO–OH monolayer, thereby enabling the ZrNO–OH monolayer to show higher ORR activity than the pristine ZrNO monolayer. Specifically, the ZrNO–OH monolayer formed in 1/4 ML-OH shows the highest ORR activity, which is also superior to the pristine ZrN. The formed hexagonal ZrNO–OH monolayer (formed in 1/4 ML-OH) gets rid of the strong oxygen adsorption characteristics of the pristine ZrN, and its RDS changed from the intrinsic sluggish last step ($*OH + H^+ + e^- \rightarrow H_2O$, ΔG_{*OH}) of ZrNO monolayer to the thermodynamically favored first step ($*O_2 + H_2O + e^- \rightarrow *OOH + OH^-$, ΔG_{*OOH}) with a much lower reaction Gibbs free energy of −0.79 eV. The two-dimensional (2D) volcano plot of the theoretical limiting potential (U_L) for ZrN with different hydroxide coverages shows the typical linear scaling relationship (Fig. 2(b)), indicating that regulating the hydroxyl coverage on the ZrN surface can effectively improve its ORR activity. The imperceptible electronic status variation of ZrNO–OH monolayers in the partial density of states (PDOS) (Fig. S8 in the ESM) indicates that the reconstructed ZrNO–OH monolayers show a negligible effect on the bulk ZrN configuration. This negligible effect is also confirmed by the Bader charge analysis (Table S1 in the ESM), which shows that the

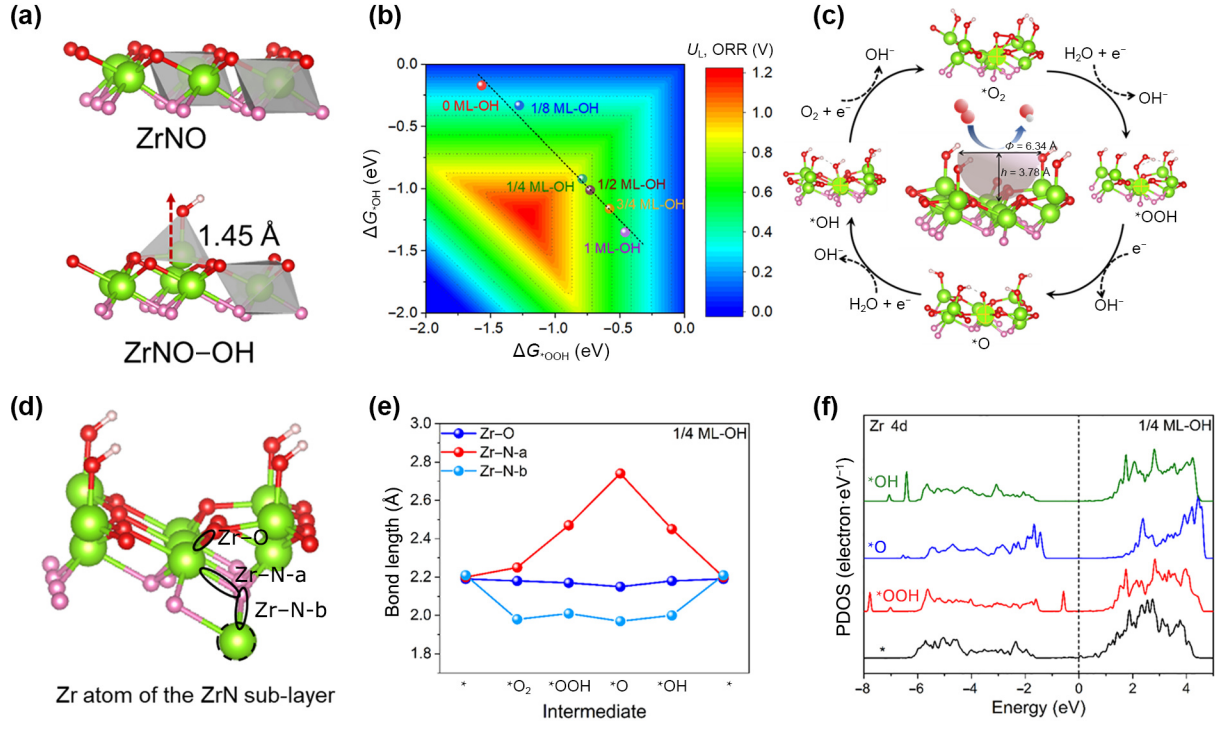

Figure 2 (a) Theoretical models of ZrNO and ZrNO–OH. (b) The ORR Gibbs free 2D volcano plot of ZrNO–OH at different hydroxide coverages. ((c)–(f)) DFT calculations for ZrNO–OH monolayer formed in 1/4 ML-OH: (c) the ORR reaction pathway and the schematic of the semi-elliptical cavity; (d) the monitored Zr–N and Zr–O bonds and (e) their variations during the ORR process; and (f) PDOS of the Zr atoms (green: Zr atom; red: O atom; pink: N atom; and grey: H atom).

charges of Zr, N, and O atoms in ZrNO and ZrNO–OH monolayers are all +2.4|e|, −1.3|e|, and −1.7|e|, respectively.

In 1/4 ML-OH, the adsorbed hydroxyl groups on the hexagonal ZrNO–OH monolayer form a semi-elliptical cavity (Fig. 2(c) and Fig. S9(a) in the ESM) with a diameter of 6.34 Å and a height of 3.78 Å, which well-matched the diameter of the oxygen molecule (3.46 Å). The electrostatic potential of this ZrNO–OH monolayer (Fig. S9(b) in the ESM) shows an obvious electron accumulation surrounding the adsorbed hydroxyl groups, suggesting its activated electronic status. We monitored the Zr–N and Zr–O bond length variations (Figs. 2(d) and 2(e)) of the hexagonal ZrNO–OH monolayer during the ORR process. The Zr–N bonds show a marked self-adaptive status, demonstrated by adjustable bond lengths to provide the optimized intermediate adsorption statuses in a complete ORR process. In contrast, the Zr–O bond lengths show a negligible fluctuation in the ORR. The self-adaptive status of the Zr–N bond can be well-explained by the rigid framework, that is, the adsorbed oxygen-related intermediates on the Zr site destroy the rigid framework of the hexagonal ZrNO–OH monolayer. This destruction activates the Zr atoms of the ZrN sub-layer, changing their spatial positions (Fig. S10(a) in the ESM) to modulate their bond lengths with the N atoms of the ZrNO–OH monolayer, thereby releasing the stress of the Zr sites applied by the oxygen intermediates and enabling ZrNO–OH monolayer to adapt different adsorption statuses. Besides, the Zr–N bond length change (Δd_{Zr-N}) shows a direct correlation with the calculated ORR U_L (Fig. S10(b) in the ESM). A larger adaptive bond contraction (6.1 Å) of ZrN with 1/4 ML-OH is associated with a higher U_L (0.79 V). This result exhibits a degree of self-adaptive stabilization during the ORR cycle. With the adsorbed *OOH, *O, and *OH intermediates, the 4d orbital of Zr atoms (Fig. 2(f) and Fig. S11 in the ESM) and the 2p orbitals of the N and O atoms (Fig. S12 in the ESM) of the ZrNO–OH monolayer positively shifted to the Fermi level. This suggests that the electron transfer abilities of the Zr, N, and O atoms situated in the ZrNO–OH monolayer are enhanced during the ORR process. It should be noted that the Zr site with the *OH intermediate shows a lower electron transfer rate than the Zr site with *OOH and *O intermediates but higher than the naked Zr site, and the Zr site with *O intermediate shows the highest electron transfer rate. This indicates that the *O transformed into *OH is the fastest ORR elementary reaction of the hexagonal ZrNO–OH monolayer, followed by the conversion of *OOH, the desorption of *OH, and the formation of *OOH, in agreement with the results of Fig. 2(b). Therefore, it can be concluded that the enhancement of ORR activity of the hexagonal ZrNO–OH monolayer formed in 1/4 ML-OH is ascribed to its self-adaptive bond length and the special protecting cavity, in which the former provides the optimized intermediate adsorption behavior and fast electron transfer, and the latter accommodates the oxygen molecule proceeding with the rapid ORR.

2.2 Catalyst characterization

Even though the ZrN has been treated in the tetramethylammonium hydroxide for a few days to induce the formation of surface hexagonal ZrNO–OH monolayer, X-ray powder diffraction (XRD) patterns (Fig. 3(a)) show that there are no differences in the pristine ZrN and the targeted ZrN@ZrNO–OH. This suggests that the resultant ZrN@ZrNO–OH derived from the organic base treatment of ZrN retains the crystal structure of the bulk ZrN. Scanning electron microscopy (SEM) (Fig. S13 in the ESM) shows that ZrN@ZrNO–OH demonstrated the same amorphous bulk morphology characteristics as the pristine ZrN. The energy dispersive spectra (EDS) mapping images (Fig. S14 in the ESM)

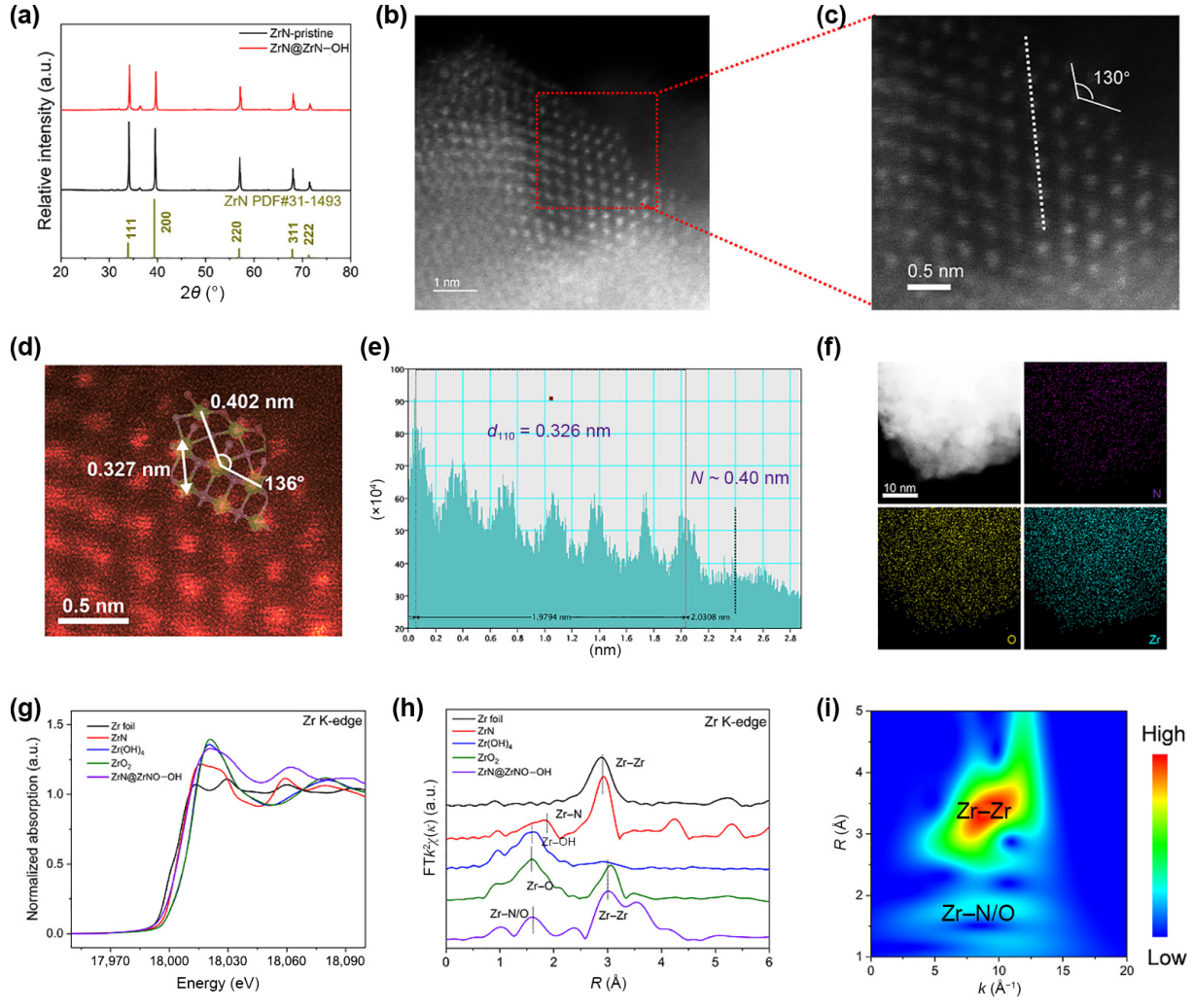

Figure 3 (a) XRD patterns of the pristine ZrN and ZrN@ZrNO–OH. ((b) and (c)) AC HAADF-STEM images of ZrN@ZrO_OH. (d) The magnified image of (c) together with a ZrNO–OH model. (e) Lattice fringes along with the arrow in (c). (f) Mapping images of ZrN@ZrNO–OH. (g) Zr K-edge XANES spectra. (h) k^2-weighted Fourier transformed EXAFS spectra for Zr. (i) Wavelet transform of the k^2-weighted EXAFS data of ZrN@ZrNO–OH.

show that Zr, N, and O elements are homogeneously dispersed on ZrN@ZrNO–OH. In addition, ZrN@ZrNO–OH shows a higher O content than the pristine ZrN, which could originate from the surface hydroxyl groups. Fourier transform infrared (FT-IR) spectra (Fig. S15 in the ESM) shows that the fingerprint peak of the stretching vibration of hydroxyl groups (~ 3735 cm^{-1}) is presented in ZrN@ZrNO–OH, and its Raman spectra (Fig. S16 in the ESM) detects the stretching vibration mode of the Zr–O (~ 663 cm^{-1}) and the Zr–O–H (~ 980 cm^{-1}) species [48, 49]. The above results suggest that the Zr–O layers and the hydroxyl groups are present in the as-prepared ZrN@ZrNO–OH. X-ray photoelectron spectroscopy (XPS) (Fig. S17 in the ESM) shows that ZrN@ZrNO–OH possesses a much higher O content than the pristine ZrN (Table S2 in the ESM). Compared to the ZrN, the binding energies of the O 1s and Zr 3d spectra of ZrN@ZrNO–OH show a red shift and a blue shift, respectively. This implies their different electronic structures and suggests the surface layer structures of ZrN@ZrNO–OH differ from the nitrogen oxide surface layer of ZrN, which is in good agreement with the DFT calculations.

To observe the surface atomic arrangement characteristics of ZrN@ZrNO–OH, which was being treated by a focused ion beam (FIB) to obtain a regular thin layer (Fig. S18 in the ESM). High-resolution transmission electron microscopy (HR-TEM) shows a distinct lattice fringe of 2.68 Å (Fig. S19 in the ESM) that belongs to the (111) plane of ZrN in ZrN@ZrNO–OH, and the lattice array of ZrN is also observed based on selected area electron diffraction (SAED) technology. The surface ZrN@ZrNO–OH monolayer shows a markedly atomic dislocation to the sub-layer (Fig. S20 in the ESM), validating that the surface monolayer differs from the sub-layer. It should be noted that the surface pristine ZrN did not present such atomic dislocation (Fig. S21 in the ESM). Aberration-corrected high-angle angular dark field-scanning TEM (AC HAADF-STEM) was performed to more clearly show this dislocation. It is observed that the surface atomic dislocation is present on ZrN@ZrNO–OH in the marked rectangular region (Fig. 3(b)). Despite FIB technology being carried out on ZrN@ZrNO–OH, its thickness, and the ultra-high imaging technical difficulties hamper fully observing the surface hexagonal monolayer, resulting in a large number of atomic buildup phases in Fig. 3(b). We further measured the lattice fringes of ZrN@ZrNO–OH and the angle of the Zr atoms of the surface ZrN–OH monolayer and the ZrN sub-layer, with the angle of 130 degrees (Fig. 3(c)), the lattice fringe of the bulk of 0.326 nm (Fig. 3(e)), and the lattice fringe between the surface ZrN–OH

monolayer and the ZrN sub-layer of 0.400 nm. These angles and lattice fringes are highly consistent with the constructed theoretical ZrN@ZrNO–OH model (Fig. 3(d)). In addition, the abundant oxygen element is observed in the mapping images (Fig. 3(f)) of ZrN@ZrNO–OH, manifesting that the ZrN has been severely modified by oxygen species and then further reconstructed into the ZrNO–OH monolayer after organic base treatment. The Zr K-edge X-ray absorption near-edge structure (XANES) was conducted to explore the chemical states and coordination environments of ZrN@ZrNO–OH with reference samples, including Zr foil, ZrO_2 and $Zr(OH)_4$ (Fig. 3(g)). The results show that both ZrN and ZrN@ZrNO–OH have a similar absorption edge position (~ 18,006.3 eV), indicating no significant change in the Zr oxidation state after treatment, consistent with the XPS results. Furthermore, the white line peak intensity of ZrN@ZrNO–OH is enhanced and shifts closer to those of ZrO_2 and $Zr(OH)_4$, demonstrating that ZrN@ZrNO–OH contains oxygen-containing groups, specifically introducing oxygen-bridged bonds and hydroxyl structures. Additionally, analysis of the extended X-ray absorption fine structure (EXAFS) data reveals that the first-shell peak for ZrN@ZrNO–OH is located at ~ 1.68 Å. This position is intermediate between that of pristine ZrN (~ 1.83 Å) and ZrO_2/$Zr(OH)_4$ (~ 1.66 Å), again indicating the incorporation of oxygen-bridged bonds and hydroxyl structures alongside the ZrN bulk structure in ZrN@ZrNO–OH. The second-shell peak appears at ~ 3.01 Å, corresponding to the main peak of Zr foil at ~ 2.91 Å (Fig. 3(h)). The wavelet transform (WT)-EXAFS contour plots reveal that Zr K-edge in ZrN@ZrNO–OH exhibits two intensity maxima around 7.5 and 8.2 $Å^{-1}$ corresponding to the Zr–N/O and Zr–N bonds (Fig. 3(i) and Fig. S22 in the ESM). These results verify that the surface ZrN monolayer successfully underwent the atomic rearrangement and reconfigured into a hexagonal ZrNO–OH monolayer.

2.3 Electrocatalytic performance

The ORR activities of the as-prepared ZrN@ZrNO–OH catalysts with different organic base (tetramethylammonium hydroxide) treatment times were measured in O_2-saturated 1 M KOH electrolyte using a typical three-electrode method in a rotating disk electrode (RDE) system. Their linear sweep voltammetry (LSV) curves (Fig. S23 in the ESM) indicate that the ZrN treated with organic bases for 5 days (ZrN@ZrNO–OH) has the highest ORR activity by demonstrating a half-wave potential ($E_{1/2}$) of 0.882 V vs. reversible hydrogen electrode (RHE). The electrochemical performance of this optimal ZrN@ZrNO–OH catalyst was further compared with those of commercial Pt/C (20%) and pristine ZrN (ZrN-pristine). The $E_{1/2}$ of the pristine ZrN and Pt/C (Fig. 4(a)) are determined to be 0.753 and 0.860 V, respectively. ZrN@ZrNO–OH shows a much higher ORR activity than the pristine ZrN and is even superior to the commercial Pt/C, suggesting the presence of the hexagonal ZrNO–OH monolayer on ZrN@ZrNO–OH possesses an unexpectedly high intrinsic ORR activity. In addition, ZrN@ZrNO–OH (59.9 $mV·dec^{-1}$) shows a lower Tafel slope than the pristine ZrN (81.2 $mV·dec^{-1}$) and Pt/C (76.8 $mV·dec^{-1}$), manifesting the faster ORR kinetics of ZrN@ZrNO–OH (Fig. 4(b)). Compared with the pristine ZrN, the ZrN@ZrNO–OH exhibits a mass activity of 2.75 $A·g^{-1}$ and a specific activity of 1.28 $mA·cm^{-1}$, up to 30 and 17 times the pristine ZrN at 0.85 V, respectively (Fig. 4(c) and Fig. S24 in the ESM). Moreover, the ZrN@ZrO–N–OH retains 94% during chronoamperometry test at 0.8 V after 10 h, far exceeding the 66% retention of Pt/C under ORR process (Fig. S25 in the ESM). The exceptional ORR performance of ZrN@ZrNO–OH shows that the reconfigured ZrNO–OH monolayer possesses a much higher intrinsic ORR activity than the inert nitrogen oxide surface layer of ZrN, as evidenced by theoretical prediction, and it highlights the critical role of the catalytic monolayer in determining the intrinsic ORR of high hardness TMNs during the electrocatalytic process (Table S3 in the ESM).

To demonstrate the application potential of ZrN@ZrNO–OH, the material was coated on carbon paper as an oxygen cathode and assembled into rechargeable liquid zinc–air batteries (ZABs) (Fig. 4(d)), with the electrolyte consisted of 6 M KOH + 0.2 M $Zn(CH_3COO)_2$. For comparison, the Pt/C-based ZABs were also assembled. The ZrN@ZrNO–OH-based ZABs show an open circuit voltage (OCV) of 1.47 V, a specific capacity (C_s) of 793 $mAh·g_{Zn}^{-1}$ at a discharge current density of 50 $mA·cm^{-2}$, and a high peak power density (P_{ZABs}) of 240 $mW·cm^{-2}$ (Figs. 4(e) and 4(f) and Fig. S25 in the ESM), far superior to that of Pt/C-based ZABs (OCV of 1.44 V, C_s of 765 $mAh·g_{Zn}^{-1}$, and P_{ZABs} of 176 $mW·cm^{-2}$). In addition, the ZrN@ZrNO–OH-based ZABs show a higher discharging voltage than Pt/C-based ZABs at different discharge current densities of 2, 5, 10, 20, 50, and 100 $mA·cm^{-2}$, delivering a good rate performance. In particular, the liquid ZrN@ZrNO–OH-based ZABs show a high voltage retention rate of 92% over 18 h discharging test at 50 $mA·cm^{-2}$, superior to the 85% of the Pt/C-based ZABs, and they can stably operate over 200 h at 10 $mA·cm^{-2}$ (Figs. 4(g) and 4(h)). Moreover, the solid ZABs based on ZrN@ZrNO–OH cathode exhibit a good stable cycling performance over 24 h (Fig. 4(h) and Fig. S26 in the ESM). The electric fan, red light-emitting diode (LED) board, and green light bulbs (Figs. 4(g) and 4(h)) are both successfully powered by the single or series-connected liquid/solid ZrN@ZrNO–OH-based ZABs, strongly verifying that the ZrN@ZrNO–OH catalyst can be a competitive cathode for the practical application of ZABs.

2.4 *In situ* spectroscopy analysis

In situ Raman and FT-IR measurements were conducted to identify the critical oxygen intermediates and to determine the specific ORR mechanism of ZrN@ZrNO–OH. *In situ* Raman spectra (Fig. 5(a)) of ZrN@ZrNO–OH show the characteristic peaks of the Zr–N bond stretching vibration mode at 491 cm^{-1}, and the D band and the G band of the used carbon substrate are also detected. The distinct peaks at ~ 977 cm^{-1} (v_1) and ~ 1066 cm^{-1} (v_2) appear in the Raman spectra, which correspond to the adsorbed hydroxyl groups on the hexagonal surface of ZrN@ZrNO–OH and the adsorbed superoxide ions ($*O_2^-$) on Zr sites, respectively [50, 51]. The presence of $*O_2^-$ and its gradually increased Raman intensity (Fig. 5(b)) confirm that the first step ($*O_2 + H_2O + e^- \rightarrow *OOH + OH^-$) is the RDS of the fabricated ZrN@ZrNO–OH, validating the DFT results. It should be noted that the peak intensities of the Zr–N bond, $*OH^-$, D band, and G band (blue shift) are gradually decreased accompanied by the applied potential varied from 0.95 to 0.35 V, which is due to the laser destroys the local structure of ZrN@ZrNO–OH and the carbon substrate (Fig. S27 in the ESM). For *in situ* FT-IR spectra (Fig. 5(c)), the detected stretching vibration of $*O_2^-$ within the range from 1007 to 1086 cm^{-1} further confirms that the RDS of ZrN@ZrNO–OH is the first step. In addition, the bending vibration mode of H_2O situated at 1633 cm^{-1} is detected, and the stretching vibration mode of OH^- is observed in the range of 2967–3727 cm^{-1}. The use of the KOH electrolyte strengthens the peak intensities of H_2O detected on the ZrN@ZrNO–OH (Fig. S28 in the ESM). The asymmetry OH^- peaks of ZrN@ZrNO–OH are deconvoluted into the K^+ ion

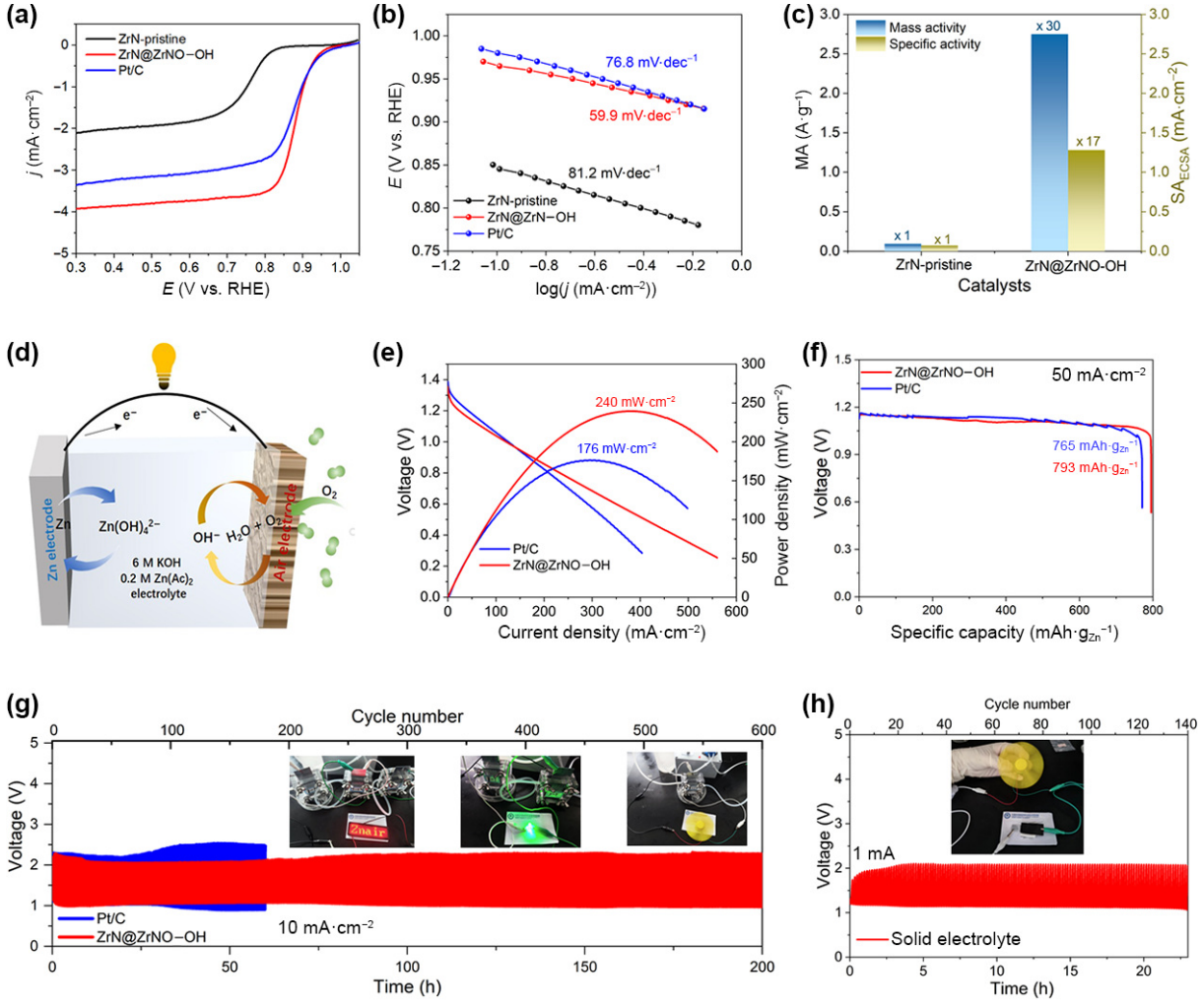

Figure 4 (a) ORR polarization curves. (b) Tafel plots. (c) Mass activity and the specific activity of the pristine ZrN and ZrN@ZrNO–OH at 0.85 V. (d) The schematic diagram of ZABs. (e) Polarization and power density curves. (f) Specific capacity normalized with the consumed zinc at 50 mA·cm^{-2}, the inset shows the photograph of the ZAB-powered LED broad. (g) Galvanostatic charge–discharge plots of ZrN@ZrNO–OH-based ZABs at 10 mA·cm^{-2}, the inset shows the photograph of the ZAB-powered LED broad, green bulb, and electric fan. (h) Galvanostatic charge–discharge plots of solid ZrN@ZrNO–OH-based ZABs at 1 mA·cm^{-2}, the inset shows the photograph of the electric fan.

hydrated water (K^+-H_2O), weak 2-coordinated hydrogen bond H_2O (2-HB-H_2O), and strong 4-coordinated hydrogen bond H_2O (4-HB-H_2O) at 3565, 3416, and 3263 cm^{-1} (Fig. 5(d)), respectively [52]. When the applied potential varied from 1.0 to 0.6 V in the FT-IR spectra of ZrN@ZrNO–OH, the contents of 4-HB-H_2O and 2-HB-H_2O were nearly stable while the content of K^+-H_2O slightly increased (Fig. 5(e)). This suggests that the O_2 reactants could dissolve in K^+-H_2O and transfer to the Zr sites of ZrN@ZrNO–OH for a rapid proton-coupled electron transfer route [53, 54]. A possible ORR route that occurred on ZrN@ZrNO–OH could be described as follows: (1) Dynamic water management that accelerates the mass transfer to the Zr sites, and (2) proton generation from water that sustains the proton inventory required for efficient ORR. *Operando* synchrotron-based X-ray absorption spectroscopy (XAS) was employed to investigate the structural evolution of ZrN@ZrNO–OH catalysts under ORR conditions (Fig. S29 in the ESM). On the one hand, the Zr oxidation state shows a slight increase (partial oxidation) as the reaction progresses (Fig. 5(f)). Upon completion of the reaction, the oxidation state decreases, returning closer to the initial state. This indicates a dynamic change occurring in the ZrN catalyst during the ORR process. On the other hand, the Zr–N/O bond length gradually decreases during the ORR reaction (Figs. 5(g) and 5(h)). This decreasing trend stops once the reaction ends. Considering that the Zr–O bond length is shorter than the Zr–N bond length (Fig. 3(h)), these *in situ* results suggest that oxygen-containing intermediates continuously adsorb during ORR, leading to an increase in the proportion of Zr–O bonds. After the reaction concludes, the trend of decreasing bond length diminishes. The Zr–Zr bond length also exhibits a similar reversible change trend, further confirming the adaptive behavior of the ZrN@ZrNO–OH surface under operating conditions. Overall, the proposed reconfiguration of the reacted surface of TMNs into an ORR-favored active surface is feasible, and we believe that this surface reconfiguration can be extended to the sulfides, phosphides, carbides, and so on.

3 Conclusions

In summary, we have precisely designed a ZrN@ZrNO–OH core–shell nanocatalyst to clarify that the surface-active monolayer and the ZrN sublayer determined the ORR activity of ZrN. Zr sites of the surface hexagonal monolayer associated with Zr atoms of the ZrN sublayer change the bond lengths of their shared Zr–N–Zr bonds during the ORR process, thereby adapting the

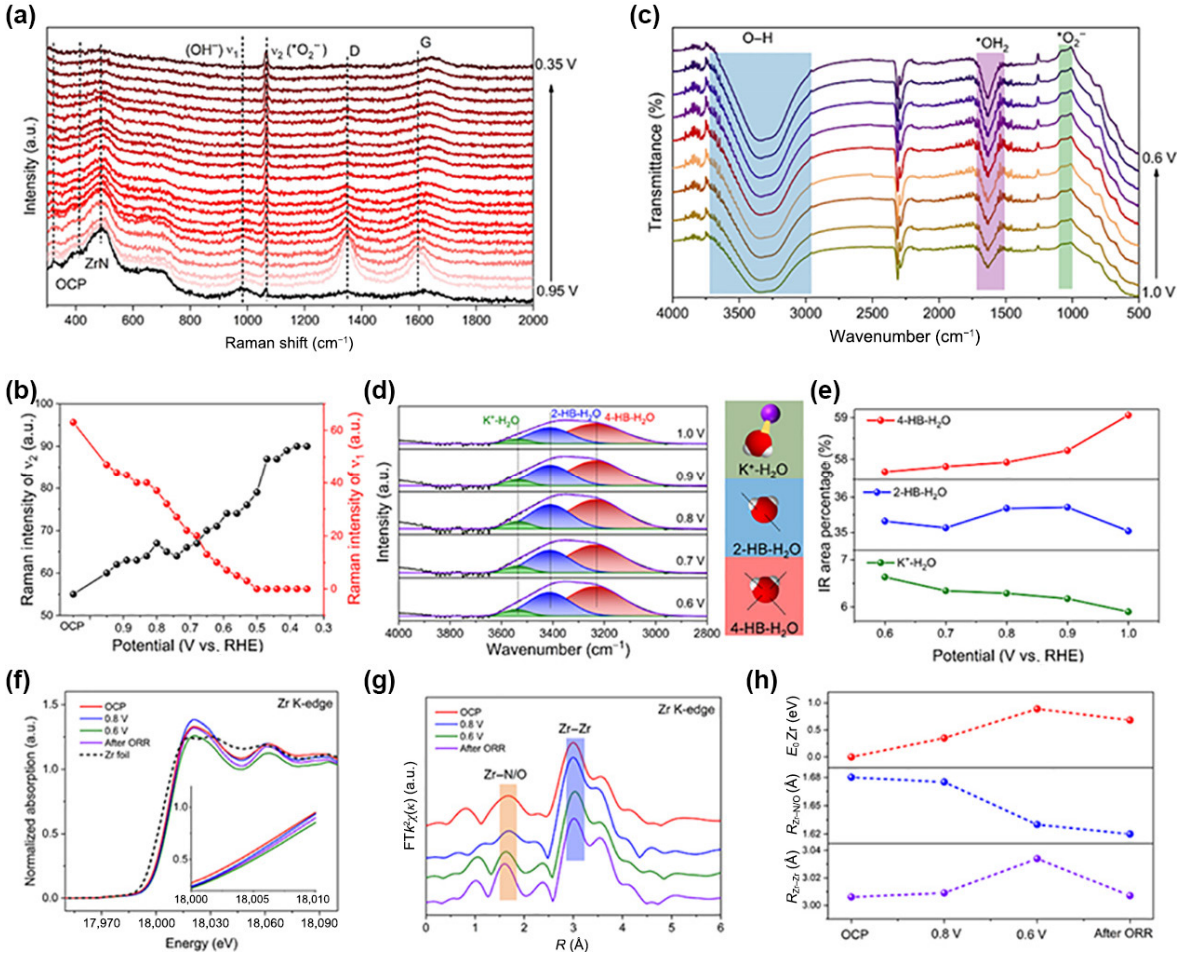

Figure 5 (a) *In situ* Raman spectra. The Raman spectra were performed in the potential range from 0.95 to 0.35 V, and the intervals of each Raman spectrum were 30 mV. (b) Raman intensity of v_1 and v_2 peaks obtained from (a). (c) *In situ* FT-IR spectra. The FT-IR spectra were recorded from 1.0 to 0.60 V, and the intervals of each FT-IR spectrum were 50 mV. ((d) and (e)) The Gaussian fitting results (d) of the OH^- species in (c) (circled by blue rectangular), which can be deconvoluted into three characteristic peaks of K^+-H_2O, 2-HB-H_2O, and 4-HB-H_2O, and their fitting areas percentage are presented in (e) (purple: K atom; red: O atom; and white: H atom). (f) *Operando* Zr K-edge XANES spectra of ZrN@ZrNO–OH under steady-state conditions from open-circuit potential (OCP), followed by applied potentials 0.8 and 0.5 V, and after ORR state. (g) *Operando* Fourier-transformed EXAFS. (h) The Zr K-edge energy, Zr–N/O, and Zr–Zr distance with as the applied potentials.

adsorption–desorption behaviors of the oxygen-related species confined in the special semi-ellipsoidal cavity and achieving rapid ORR kinetics. The resultant ZrN@ZrNO–OH shows a higher ORR activity and a better practical ZABs performance than benchmark Pt/C. *In situ* spectroscopy validated that the RDS of ZrN@ZrNO–OH is the step of $*O_2$ combined with one electron and hydrogen to form *OOH intermediate, as evidenced by DFT calculations. This work establishes a fundamental insight into the catalytic monolayers and provides a pathway for the rational design of highly efficient catalysts for clean energy technology.

Electronic Supplementary Material: Supplementary material (the synthesis of ZrN@ZrNO–OH, various characterization techniques (XRD, XPS, Raman, SEM, FIB‐SEM, HR‐TEM, HAADF‐STEM, FT‐IR, and XAFS), DFT calculations, and *in situ* experiments) is available in the online version of this article at https://doi.org/10.26599/NR.2026.94908558.

Data availability

All data needed to support the conclusions in the paper are presented in the manuscript and the Electronic Supplementary Material. Additional data related to this paper may be requested from the corresponding author upon request.

Acknowledgements

We acknowledge financial support from the National Key R&D Program of China (No. 2022YFB2402600), the National Natural Science Foundation of China (Nos. 52125105, 52273312, and 52271233), and Shenzhen Science and Technology Planning Project (Nos. JSGG20220831104004008, SGDX20230116092055008, KJZD20241122161900001, and JCYJ20220531100405012).

Declaration of competing interest

All the contributing authors report no conflict of interests in this work.

Author contribution statement

X. L. and R. H. G. are equally contributed to this work. X. L.: Investigation, experimental design, data curation, software, writing manuscripts. R. H. G.: Formal analysis, data curation, review. X. D.

S.: Resources. J. X. W.: Validation. Y. P. Z.: Software, supervision, writing manuscripts, funding acquisition. C. L. J: Review. Y. B. T.: Resources, supervision, funding acquisition. All the authors have approved the final manuscript.

Use of AI statement

None.

References

[1] Shao, M. H.; Chang, Q. W.; Dodelet, J. P.; Chenitz, R. Recent advances in electrocatalysts for oxygen reduction reaction. *Chem. Rev.* **2016**, *116*, 3594–3657.

[2] Han, A. L.; Sun, W. M.; Wan, X.; Cai, D. D.; Wang, X. J.; Li, F.; Shui, J. L.; Wang, D. S. Construction of Co_4 atomic clusters to enable Fe–N_4 motifs with highly active and durable oxygen reduction performance. *Angew. Chem., Int. Ed.* **2023**, *62*, e202303185.

[3] Qi, Y. G.; Yao, K. X.; Liang, Q.; Zhou, X. Y.; Liu, M. Q.; Li, W. W.; Liu, F. X.; Jiang, Z.; Gu, Q. H.; Chen, Z. J. et al. Asymmetric B-coordination stimulated high-spin cobalt boosts ORR. *Nano Res.* **2025**, *18*, 94907278.

[4] Lei, X.; Tang, Q. Y.; Zheng, Y. P.; Kidkhunthod, P.; Zhou, X. L.; Ji, B. F.; Tang, Y. B. High-entropy single-atom activated carbon catalysts for sustainable oxygen electrocatalysis. *Nat. Sustain.* **2023**, *6*, 816–826.

[5] Ji, B. F.; Gou, J. L.; Zheng, Y. P.; Zhou, X. L.; Kidkhunthod, P.; Wang, Y. H.; Tang, Q. Y.; Tang, Y. B. Metalloid-cluster ligands enabling stable and active FeN_4–Te_n motifs for the oxygen reduction reaction. *Adv. Mater.* **2022**, *34*, 2202714.

[6] Gou, J. L.; Lei, X.; Ji, B. F.; Zhang, S. S.; Zheng, Y. P.; Tang, Y. B. Adaptive morphing of hydroxyl groups on covalency competing spinel oxides boosting oxygen evolution reactions. *ACS Catal.* **2025**, *15*, 2053–2062.

[7] Jaganmohan, M. *Mine Production of Platinum Worldwide from 2010 to 2024* [Online]. https://www.statista.com/statistics/1170691/mine-production-of-platinum-worldwide/(2024) (accessed Jun 1, 2025).

[8] Ji, N. N.; Sheng, H. Y.; Liu, S. L.; Zhang, Y. Y.; Sun, H. F.; Wei, L. Z.; Tian, Z. Q.; Jiang, P.; Chen, Q. W.; Su, J. W. Boosting oxygen reduction in acidic media through integration of Pt–Co alloy effect and strong interaction with carbon defects. *Nano Res.* **2024**, *17*, 7900–7908.

[9] Chen, R.; Shu, T.; Zhao, F. L.; Li, Y. F.; Yang, X. T.; Li, J. W.; Zhang, D. L.; Gan, L. Y.; Yao, K. X.; Yuan, Q. $PtCu_3$ nanoalloy@porous PWO_x composites with oxygen container function as efficient ORR electrocatalysts advance the power density of room-temperature hydrogen–air fuel cells. *Nano Res.* **2022**, *15*, 9010–9018.

[10] Du, L.; Prabhakaran, V.; Xie, X. H.; Park, S.; Wang, Y.; Shao, Y. Y. Low-PGM and PGM-free catalysts for proton exchange membrane fuel cells: Stability challenges and material solutions. *Adv. Mater.* **2021**, *33*, 1908232.

[11] Núñez, M.; Lansford, J. L.; Vlachos, D. G. Optimization of the facet structure of transition-metal catalysts applied to the oxygen reduction reaction. *Nat. Chem.* **2019**, *11*, 449–456.

[12] Chen, Y. X.; Meng, Z. H.; Wei, X. L.; Wu, M. J.; Xiong, Y. F.; Tang, H. B.; Wang, R.; Tian, T.; Wang, D. S.; Tang, H. L. Tellurium–nitrogen–carbon support boosting platinum catalysis in high-efficiency proton exchange membrane fuel cells. *Angew. Chem., Int. Ed.* **2025**, *64*, e202512315.

[13] Niu, W. H.; Pakhira, S.; Cheng, G. M.; Zhao, F.; Yao, N.; Mendoza-Cortes, J. L.; Koel, B. E. Reaction-driven restructuring of defective $PtSe_2$ into ultrastable catalyst for the oxygen reduction reaction. *Nat. Mater.* **2024**, *23*, 1704–1711.

[14] Wang, C. B.; Li, M. K.; Li, P.; Fan, K. C.; Liu, P. R.; Zhan, T. R.; Li, B.; Zong, L. B.; Wang, L. Rigid ligand confined rapid synthesis of dual single-atomic sites on carbon black for enhanced oxygen depolarized cathodes. *Nano Res.* **2026**, *19*, 94907794.

[15] Shen, J.; Tang, M. H.; Shi, Z. H.; Guan, S. Y.; Shi, Y. J.; Zhuang, Z. C.; Li, R. Z.; Yang, J. R.; He, D. P.; Liu, B. Z. et al. Efficient generation of negative hydrogen with bimetallic-ternary-structured catalysts for nitrobenzene hydrogenation. *Angew. Chem., Int. Ed.* **2025**, *64*, e202423626.

[16] Guan, S. Y.; Yuan, Z. L.; Zhao, S. Q.; Zhuang, Z. C.; Zhang, H. H.; Shen, R. F.; Fan, Y. P.; Li, B. J.; Wang, D. S.; Liu, B. Z. Efficient hydrogen generation from ammonia borane hydrolysis on a tandem ruthenium–platinum–titanium catalyst. *Angew. Chem., Int. Ed.* **2024**, *63*, e202408193.

[17] Wang, H.; Li, J. M.; Li, K.; Lin, Y. P.; Chen, J. M.; Gao, L. J.; Nicolosi, V.; Xiao, X.; Lee, J. M. Transition metal nitrides for electrochemical energy applications. *Chem. Soc. Rev.* **2021**, *50*, 1354–1390.

[18] Yang, Z. G.; Xu, H. M.; Shuai, T. Y.; Zhan, Q. N.; Zhang, Z. J.; Huang, K.; Dai, C. L.; Li, G. R. Recent progress in the synthesis of transition metal nitride catalysts and their applications in electrocatalysis. *Nanoscale* **2023**, *15*, 11777–11800.

[19] Wu, F. M.; Lei, X.; Pan, X. W.; Nie, H. F.; Xiao, Q.; Zhou, X. L.; Deng, W.; Kidkhunthod, P.; Padchasri, J.; Tunmee, S. et al. Synergistic mechanism of nanochannels and chain migration in bioinspired solid-state gel electrolytes for ultrahigh-rate, long-life flexible tin–air batteries. *Angew. Chem., Int. Ed.* **2025**, *64*, e202517649.

[20] Soto, J.; Li, Q. H.; Shi, Z. X.; Molina Villarino, A.; Muller, D.; Abruña, H. D. Surface modulation insights of high-performing Ni–Fe nitride fuel cell and electrolyzer electrocatalysts. *Chem. Mater.* **2025**, *37*, 153–166.

[21] Tian, X. L.; Lu, X. F.; Xia, B. Y.; Lou, X. W. Advanced electrocatalysts for the oxygen reduction reaction in energy conversion technologies. *Joule* **2020**, *4*, 45–68.

[22] Ji, B. F.; Gou, J. L.; Zheng, Y. P.; Pu, X. H.; Wang, Y. H.; Kidkhunthod, P.; Tang, Y. B. Coordination chemistry of large-sized yttrium single-atom catalysts for oxygen reduction reaction. *Adv. Mater.* **2023**, *35*, 2300381.

[23] Pan, Z. C.; Xiao, Y. H.; Fu, Z. G.; Zhan, G. H.; Wu, S. K.; Xiao, C. M.; Hu, G. H.; Wei, Z. G. Hollow and porous titanium nitride nanotubes as high-performance catalyst supports for oxygen reduction reaction. *J. Mater. Chem. A* **2014**, *2*, 13966–13975.

[24] Chen, S. H.; Ye, C. L.; Wang, Z. W.; Li, P.; Jiang, W. J.; Zhuang, Z. C.; Zhu, J. X.; Zheng, X. B.; Zaman, S.; Ou, H. H. et al. Selective CO_2 reduction to ethylene mediated by adaptive small-molecule engineering of copper-based electrocatalysts. *Angew. Chem., Int. Ed.* **2023**, *62*, e202315621.

[25] Yang, Y.; Zeng, R.; Xiong, Y.; DiSalvo, F. J.; Abruña, H. D. Cobalt-based nitride-core oxide-shell oxygen reduction electrocatalysts. *J. Am. Chem. Soc.* **2019**, *141*, 19241–19245.

[26] Zhang, H.; Liu, M. H.; Cheng, W. R.; Li, Y. L.; Zhou, W. L.; Su, H.; Zhao, X.; Yao, P.; Liu, Q. H. Metallic Ni_3N quantum dots as a synergistic promoter for NiO nanosheet toward efficient oxygen reduction electrocatalysis. *J. Phys. Chem. C* **2019**, *123*, 8633–8639.

[27] Cao, B. F.; Veith, G. M.; Diaz, R. E.; Liu, J.; Stach, E. A.; Adzic, R. R.; Khalifah, P. G. Cobalt molybdenum oxynitrides: Synthesis, structural characterization, and catalytic activity for the oxygen reduction reaction. *Angew. Chem., Int. Ed.* **2013**, *52*, 10753–10757.

[28] Yuan, Y.; Wang, J. C.; Adimi, S.; Shen, H. J.; Thomas, T.; Ma, R. G.; Attfield, J. P.; Yang, M. H. Zirconium nitride catalysts surpass platinum for oxygen reduction. *Nat. Mater.* **2020**, *19*, 282–286.

[29] Maekawa, Y.; Ishihara, A.; Kim, J. H.; Mitsushima, S.; Ota, K. I. Catalytic activity of zirconium oxynitride prepared by reactive sputtering for ORR in sulfuric acid. *Electrochem. Solid-State Lett.* **2008**, *11*, B109.

[30] Luo, J. M.; Tian, X. L.; Zeng, J. H.; Li, Y. W.; Song, H. Y.; Liao, S. J. Limitations and improvement strategies for early-transition-metal

nitrides as competitive catalysts toward the oxygen reduction reaction. *ACS Catal.* **2016**, *6*, 6165–6174.

[31] Zeng, R.; Li, H. Q.; Shi, Z. X.; Xu, L.; Meng, J. H.; Xu, W. X.; Wang, H. S.; Li, Q. H.; Pollock, C. J.; Lian, T. Q. et al. Origins of enhanced oxygen reduction activity of transition metal nitrides. *Nat. Mater.* **2024**, *23*, 1695–1703.

[32] Hu, H. S.; Wang, X. L.; Attfield, J. P.; Yang, M. H. Metal nitrides for seawater electrolysis. *Chem. Soc. Rev.* **2024**, *53*, 163–203.

[33] Cai, J.; Wei, L. Y.; Liu, J.; Xue, C. W.; Chen, Z. X.; Hu, Y. X.; Zang, Y. J.; Wang, M. X.; Shi, W. J.; Qin, T. et al. Two-dimensional crystalline platinum oxide. *Nat. Mater.* **2024**, *23*, 1654–1663.

[34] Wang, X. L.; Hu, H. S.; Yan, X. H.; Zhang, Z. R.; Yang, M. H. Activating interfacial electron redistribution in lattice-matched biphasic Ni_3N–Co_3N for energy-efficient electrocatalytic hydrogen production via coupled hydrazine degradation. *Angew. Chem., Int. Ed.* **2024**, *63*, e202401364.

[35] Deng, Y. P.; Jiang, Y.; Liang, R. L.; Zhang, S. J.; Luo, D.; Hu, Y. F.; Wang, X.; Li, J. T.; Yu, A. P.; Chen, Z. W. Dynamic electrocatalyst with current-driven oxyhydroxide shell for rechargeable zinc–air battery. *Nat. Commun.* **2020**, *11*, 1952.

[36] Calle-Vallejo, F.; Tymoczko, J.; Colic, V.; Vu, Q. H.; Pohl, M. D.; Morgenstern, K.; Loffreda, D.; Sautet, P.; Schuhmann, W.; Bandarenka, A. S. Finding optimal surface sites on heterogeneous catalysts by counting nearest neighbors. *Science* **2015**, *350*, 185–189.

[37] Zhao, Z. J.; Liu, S. H.; Zha, S. J.; Cheng, D. F.; Studt, F.; Henkelman, G.; Gong, J. L. Theory-guided design of catalytic materials using scaling relationships and reactivity descriptors. *Nat. Rev. Mater.* **2019**, *4*, 792–804.

[38] Wang, X. Z.; Muneshwar, T. P.; Fan, H. Q.; Cadien, K.; Luo, J. L. Achieving ultrahigh corrosion resistance and conductive zirconium oxynitride coating on metal bipolar plates by plasma enhanced atomic layer deposition. *J. Power Sour.* **2018**, *397*, 32–36.

[39] Xu, J.; Xu, S.; Munroe, P.; Xie, Z. H. A ZrN nanocrystalline coating for polymer electrolyte membrane fuel cell metallic bipolar plates prepared by reactive sputter deposition. *RSC Adv.* **2015**, *5*, 67348–67356.

[40] Lyu, L. L.; Hu, X.; Lee, S.; Fan, W. Q.; Kim, G.; Zhang, J. L.; Zhou, Z.; Kang, Y. M. Oxygen reduction kinetics of Fe–N–C single atom catalysts boosted by pyridinic N vacancy for temperature-adaptive Zn–air batteries. *J. Am. Chem. Soc.* **2024**, *146*, 4803–4813.

[41] Aizpuru, J.; Céspedes, E.; De La Fuente, J. L. G.; De Andrés, A.; Prieto, C.; Retuerto, M.; Rojas, S.; Bueno, S. V.; Climent-Pascual, E. ZrN-based multilayers prepared by reactive sputtering as coatings for electrode plates of proton exchange membrane water electrolyzers. *ACS Appl. Mater. Interfaces* **2024**, *16*, 66470–66481.

[42] Kreider, M. E.; Stevens, M. B.; Liu, Y. Z.; Patel, A. M.; Statt, M. J.; Gibbons, B. M.; Gallo, A.; Ben-Naim, M.; Mehta, A.; Davis, R. C. et al. Nitride or oxynitride? Elucidating the composition-activity relationships in molybdenum nitride electrocatalysts for the oxygen reduction reaction. *Chem. Mater.* **2020**, *32*, 2946–2960.

[43] Chen, C.; Yang, R.; Zhu, J.; Yao, W. J.; Tang, Y. B. Superior sodium metal anodes enabled by 3D hierarchical metallic scaffolds with enhanced sodiophilicity. *Adv. Sci.* **2025**, *12*, 2500756.

[44] Magnussen, O. M.; Groß, A. Toward an atomic-scale understanding of electrochemical interface structure and dynamics. *J. Am. Chem. Soc.* **2019**, *141*, 4777–4790.

[45] Adachi, J.; Kurosaki, K.; Uno, M.; Yamanaka, S. Thermal and electrical properties of zirconium nitride. *J. Alloys Compd.* **2005**, *399*, 242–244.

[46] Liu, H.; Zhang, D.; Holmes, S. M.; D'Agostino, C.; Li, H. Origin of the superior oxygen reduction activity of zirconium nitride in alkaline media. *Chem. Sci.* **2023**, *14*, 9000–9009.

[47] Li, H.; Kelly, S.; Guevarra, D.; Wang, Z. B.; Wang, Y.; Haber, J. A.; Anand, M.; Gunasooriya, G. T. K. K.; Abraham, C. S.; Vijay, S. et al. Analysis of the limitations in the oxygen reduction activity of transition metal oxide surfaces. *Nat. Catal.* **2021**, *4*, 463–468.

[48] You, M. M.; Li, Y. J.; Zhang, H. K.; Lin, Z. D.; Li, J. J.; Li, X. Y.; Liu, J. Q. The mechanism of phase transition induced by oxygen doping in zirconium nitride thin films. *J. Mater. Sci.* **2022**, *57*, 18456–18467.

[49] Constable, C. P.; Yarwood, J.; Münz, W. D. Raman microscopic studies of PVD hard coatings. *Surf. Coat. Technol.* **1999**, *116–119*, 155–159.

[50] Bo, X.; Hocking, R. K.; Zhou, S.; Li, Y. B.; Chen, X. J.; Zhuang, J. C.; Du, Y.; Zhao, C. Capturing the active sites of multimetallic (oxy)hydroxides for the oxygen evolution reaction. *Energy Environ. Sci.* **2020**, *13*, 4225–4237.

[51] Wei, J.; Xia, D. S.; Wei, Y. P.; Zhu, X. Y.; Li, J.; Gan, L. Probing the oxygen reduction reaction intermediates and dynamic active site structures of molecular and pyrolyzed Fe–N–C electrocatalysts by *in situ* Raman spectroscopy. *ACS Catal.* **2022**, *12*, 7811–7820.

[52] Wan, Y. C.; Tang, Y. X.; Zuo, Y. Z.; Sun, K. A.; Zhuang, Z. W.; Zheng, Y.; Yan, W.; Zhang, J. J.; Lv, R. T. Interfacial hydrogen-bond modulation of dynamic catalysts for nitrate electroreduction to ammonia. *Energy Environ. Sci.* **2025**, *18*, 7460–7469.

[53] Ji, S. G.; Kim, M. M.; Han, M. H.; Cho, J.; Son, Y.; Kim, Y. Y.; Jeong, J.; Kim, Z. H.; Chae, K. H.; Oh, H. S. et al. Alkali metal cations act as homogeneous cocatalysts for the oxygen reduction reaction in aqueous electrolytes. *Nat. Catal.* **2024**, *7*, 1330–1338.

[54] Wu, Q.; Xu, Z. J. Mechanistic insights into cation effects in electrolytes for electrocatalysis. *Angew. Chem., Int. Ed.* **2025**, *64*, e202505022.